Title	Influence of Black Hole Kick Velocity on Microlensing Distributions
Author(s)	Koshimoto, Naoki; Kawanaka, Norita; Tsuna, Daichi
Citation	Astrophysical Journal. 2024, 973(1), p. 5
Version Type	VoR
URL	https://hdl.handle.net/11094/98351
rights	This article is licensed under a Creative Commons Attribution 4.0 International License.
Note	

Influence of Black Hole Kick Velocity on Microlensing Distributions

Naoki Koshimoto[1] , Norita Kawanaka[2,3,4] , and Daichi Tsuna[5,6]

[1] Department of Earth and Space Science, Graduate School of Science, Osaka University, Toyonaka, Osaka 560-0043, Japan
[2] National Astronomical Observatory of Japan (NAOJ), 2-21-1, Osawa, Mitaka, Tokyo 181-8588, Japan
[3] Department of Physics, Graduate School of Science, Tokyo Metropolitan University, 1-1 Minami-Osawa, Hachioji-shi, Tokyo 192-0397, Japan
[4] Center for Gravitational Physics and Quantum Information, Yukawa Institute for Theoretical Physics, Kyoto University, Kyoto 606-8502, Japan
[5] TAPIR, Mailcode 350-17, California Institute of Technology, Pasadena, CA 91125, USA
[6] Research Center for the Early Universe (RESCEU), Graduate School of Science, The University of Tokyo, 7-3-1 Hongo, Bunkyo-ku, Tokyo 113-0033, Japan

Abstract

The natal kick velocity distribution for black holes (BHs) is unknown regardless of its importance for understanding the BH formation process. Gravitational microlensing is a unique tool for studying the distribution of BHs in our Galaxy, and the first isolated stellar-mass BH event, OGLE-2011-BLG-0462/MOA-2011-BLG-191 (OB110462), was recently identified by astrometric microlensing. This study investigates how the natal kick velocity for Galactic BHs affects the microlensing event rate distribution. We consider a Maxwell distribution with various average kick velocities, as well as the consequent variation of the spatial distribution of BHs. We find that the event rate for the BH lenses toward the Galactic bulge decreases as $v_{\rm avg}$ increases, mainly due to the scale height inflation. We focus on the unique microlensing parameters measured for OB110462, with microlens parallax $\pi_{\rm E}$ larger than 0.06 for its long timescale of $t_{\rm E} > 200$ days. We calculate the expected number of BH events occurring with parameters similar to OB110462 during the OGLE-IV survey by Mróz et al. and compare it with the actual number that occurred, at least one. Our fiducial model predicts 0.52, 0.38, 0.18, 0.042, and 4.0×10^{-3} events occurring for $v_{\rm avg} = 25, 50, 100, 200$, and 400 km s^{-1}, respectively, which suggests that the average kick velocity is likely to be $v_{\rm avg} \lesssim 100$ km s^{-1}. The expected number smaller than unity even at maximum might indicate our luck in finding OB110462, which can be tested with future surveys by, e.g., the Roman Space Telescope.

Unified Astronomy Thesaurus concepts: Stellar mass black holes (1611); Gravitational microlensing (672)

1. Introduction

Black holes (BHs) are the remnants of massive stars after their gravitational collapse. Considering the stellar evolution theory, initial mass function, and star formation rate in our Galaxy, one can estimate the number of Galactic stellar-mass BHs as 10^{8-9} (Shapiro & Teukolsky 1983; van den Heuvel 1992; Samland 1998; Caputo et al. 2017; Lamberts et al. 2018; Olejak et al. 2020).

Among Galactic BHs, those in binary systems with mass transfer from their companions can be detected as X-ray binaries, and several dozens of X-ray binaries have been confirmed to contain BHs so far (Corral-Santana et al. 2016). From the mass distribution of BHs in transient low-mass X-ray binaries, it has been implied that compact objects with mass of 3–5 $M_\odot$ are absent (Özel et al. 2010; Farr et al. 2011). If this "lower mass gap" (Bailyn et al. 1998) is not an observational bias but intrinsic, it should have some hints about the process of BH formation after the core collapse of a massive star (Fryer et al. 2012). In other studies, the spatial distribution of BH X-ray binaries is investigated (Gandhi et al. 2020; Jonker et al. 2021). Assuming that BH X-ray binaries originate from the Galactic plane, their Galactic heights (i.e., the distances from the Galactic plane) reflect the strength of kicks on BHs at their births. However, the Galactic BHs appearing in the analyses above are significantly biased to those contained in close binary systems, observed as bright X-ray binaries. In order to draw conclusions

about the BH formation processes in our Galaxy in a more general way, one should also investigate the statistical properties of BH binaries without mass transfer because of their large orbital separation (i.e., noninteracting BH binaries), and BHs without companions (i.e., isolated BHs). As for noninteracting BH binaries, they can be detected via astrometric observations of their luminous companions' motions. There are some studies that have estimated the number of noninteracting BH binaries detectable by the astrometric satellite Gaia (Breivik et al. 2017; Kawanaka et al. 2017; Mashian & Loeb 2017; Kinugawa & Yamaguchi 2018; Yalinewich et al. 2018; Yamaguchi et al. 2018; Andrews et al. 2019; Shao & Li 2019; Shikauchi et al. 2020; Wiktorowicz et al. 2020; Chawla et al. 2022; Shikauchi et al. 2022, 2023). So far, three sources have been identified as noninteracting BH binaries from the Gaia data (Chakrabarti et al. 2023; El-Badry et al. 2023a, 2023b; Tanikawa et al. 2023; Gaia Collaboration et al. 2024), and some candidates of BH binaries have been reported (Andrews et al. 2022; Shahaf et al. 2023).

Another important subset of Galactic BHs is those without companions, i.e., isolated BHs. Detection of isolated BHs is much more difficult than those in binaries. One of the methods is to detect the emission from an isolated BH accreting surrounding medium (Shvartsman 1971; Meszaros 1975; Grindlay 1978; Carr 1979; McDowell 1985; Campana & Pardi 1993; Fujita et al. 1998; Popov & Prokhorov 1998; Armitage & Natarajan 1999; Agol & Kamionkowski 2002; Chisholm et al. 2003; Maccarone 2005; Mii & Totani 2005; Barkov et al. 2012; Fender et al. 2013; Ioka et al. 2017; Matsumoto et al. 2018; Tsuna et al. 2018; Tsuna & Kawanaka 2019; Kimura et al. 2021), although no isolated accreting BH in our Galaxy has been unambiguously detected so far.

Another promising method to find isolated BHs is to detect the microlensing events. When a massive compact object passes in front of a background star, the stellar light is deflected due to general relativistic effects, and an apparent magnification (photometric microlensing) and/or a positional shift (astrometric microlensing) of a background star will be temporarily observed (Einstein 1936; Paczynski 1986; Hog et al. 1995; Miyamoto & Yoshii 1995; Walker 1995). Some previous studies propose to find Galactic BHs by the observations of microlensing events (Gould 2000; Agol et al. 2002; Sartore & Treves 2010). There are four quantities that are involved in each microlensing event: the lens mass M_L, the distance to the lens D_L, the distance to the source D_S, and the relative proper motion between the lens and the source μ_{rel}. In the case of photometric microlensing, the duration of an event is described by the Einstein radius crossing time,

$$t_E = \frac{\theta_E}{\mu_{rel}}, \qquad (1)$$

where θ_E is the angular Einstein radius given by

$$\theta_E = \sqrt{\kappa M_L \pi_{rel}}, \qquad (2)$$

with $\kappa = 8.144$ mas $M_\odot^{-1}$ and $\pi_{rel} = 1$ au $(D_L^{-1} - D_S^{-1})$. The Einstein radius crossing time is commonly measured in most microlensing events. In a long-timescale event such as the one due to a BH lens, the microlens parallax given by $\pi_E \equiv \pi_{rel}/\theta_E$ can be constrained via the parallax effect. Considering that in most cases, the distance from a source is well constrained (e.g., $D_S \simeq 8$ kpc when the survey is toward the Galactic bulge), there is still a parameter degeneracy in a parallax event, which makes it difficult to deduce the lens properties from photometric microlensing. This degeneracy can be broken by the detection of astrometric microlensing (Bennett et al. 2002; Lu et al. 2016; Kains et al. 2017; Sahu et al. 2017), which enables us to measure the mass of a lens object as well as its distance. Recently, thanks to the combination of photometric and astrometric lensing observations, the mass of an isolated BH acting as a lens was measured for the first time (OGLE-2011-BLG-0462/MOA-2011-BLG-191; Lam et al. 2022, 2022; Mróz et al. 2022; Sahu et al. 2022; Lam & Lu 2023). Some studies have tried to constrain the origin or formation channel of this isolated BH with observed mass and velocity (Andrews & Kalogera 2022; Vigna-Gómez & Ramirez-Ruiz 2023). Even if astrometric microlensing events are not detected extensively, a number of detections of photometric microlensing events can give some constraints on the mass function, spatial distribution, and velocity distribution of Galactic BHs, which will provide insights into the physical processes occurring at the formation of BHs such as mass ejection, natal kick, and so on (Wyrzykowski et al. 2016; Lam et al. 2020; Wyrzykowski & Mandel 2020; Mróz & Wyrzykowski 2021; Mroz et al. 2021; Rose et al. 2022; Perkins et al. 2024). Among them, the natal kick velocity distribution is of great importance for understanding the BH formation process. It is expected that the compact remnants of massive stars (i.e., neutron stars and BHs) suffer from a kick at their births to have a peculiar velocity, possibly due to the asymmetry in the supernova explosion (for a review, see Lai et al. 2001; for recent studies see Janka 2013; Burrows et al. 2023, 2024; Janka & Kresse 2024). From the measurements of proper motions of young pulsars, the kick velocity of a neutron star is up to a few hundred kilometers per second (Hobbs et al. 2005). Although there are some works on the kick velocities of Galactic BHs based on the observations of X-ray binaries (Willems et al. 2005; Fragos et al. 2009; Wong et al. 2012, 2014; Banagiri et al. 2023; Kimball et al. 2023; Zhao et al. 2023), the kick velocity distribution of Galactic BHs is still uncertain both observationally and theoretically. Very recently, Sweeney et al. (2024) predicted the number of observable microlensing events caused by Galactic-isolated BHs or neutron stars, making use of the population synthesis by Sweeney et al. (2022), which takes into account the spatial distributions of Galactic compact objects affected by natal kicks at their births. Their results are obtained from a single kick velocity distribution model that is based on the observations of the neutron stars' proper motions (Igoshev 2020; Igoshev et al. 2021), and the assumption that natal kicks impart the same momentum to compact objects.

In this study, we predict the parameter distributions of observable photometric microlensing events caused by Galactic-isolated BHs. Especially, the difference in the kick velocity distributions gives rise to differences in the spatial distributions of BHs in the Galaxy, which affects the detectability of microlensing events caused by BHs as well as their durations and parallaxes. We investigate the dependence of these observational properties on the kick velocity distribution. In addition, we compare our results with past observations, including OGLE-2011-BLG-0462/MOA-2011-BLG-191, the microlensing event that is confirmed to be caused by a BH lens.

The structure of this paper is as follows. In Section 2, we describe the Galactic model, the model of BH natal kicks, and the model of the spatial distribution of BHs employed in this study. The influence of natal kicks on the parameter distributions of microlensing events is investigated in Section 3. Section 4 is dedicated to the implication of our results on the natal kick velocity of the BH from the astrometric microlensing event OGLE-2011-BLG-0462/MOA-2011-BLG-191. In Section 5, we discuss the uncertainties involved in the model, the possibility that OGLE-2011-BLG-0462/MOA-2011-BLG-191 is a "lucky" event, and comparisons with previous studies. We summarize and conclude in Section 6.

2. Model

In this paper, we refer to a combination of the stellar mass function, stellar density distribution, and stellar velocity distribution in our Galaxy as a Galactic model. We use the Galactic model developed by Koshimoto et al. (2021, hereafter K21) to simulate the microlensing events toward the Galactic bulge and we take their $E + E_X$ model. The model consists of a multicomponent thin disk, a thick disk, and a barred bulge with an X-shaped structure. It is optimized for use in microlensing studies toward the Galactic bulge region. It is fitted to various observational distributions toward the Galactic bulge, including OGLE-III red clump star count data (Nataf et al. 2013), VIRAC proper-motion data (Smith et al. 2018; Clarke et al. 2019), BRAVA radial velocity data (Rich et al. 2007; Kunder et al. 2012), and OGLE-IV star count and microlensing rate data (Mróz et al. 2017, 2019). It is particularly notable that this model is confirmed to reproduce
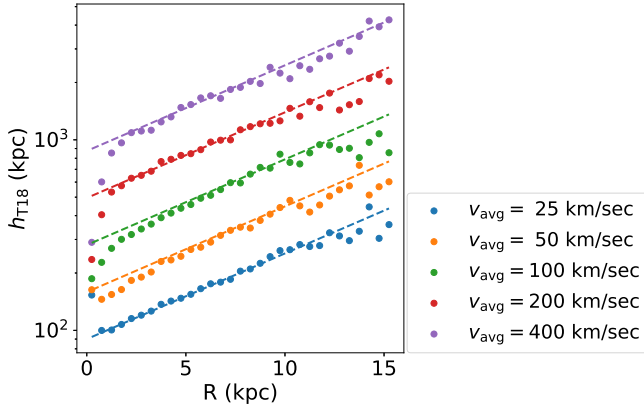
Figure 1. Scale height distribution of the BH density profile in Tsuna et al. (2018)'s numerical model as a function of the radius from the Galactic center and the average velocity of the BH population. Dashed lines show our analytical model approximation fitted to the numerical model at $1.25 < R/\text{kpc} < 8.75$.

the OGLE-IV t_E distribution (Mróz et al. 2017, 2019), which enables us to constrain the kick velocity for BHs in Section 4.

2.1. BH Mass Function

The model by K21 combines the stellar initial mass function, which has a power-law shape of $dN/dM_{\text{ini}} \propto M_{\text{ini}}^{-2.32}$ at $M_{\text{ini}} > 0.86 M_\odot$, with the stellar age distribution and the initial-final mass relation (IFMR) by Lam et al. (2020) to obtain the present-day mass function for remnant objects. For the age distribution, a time-dependent star formation rate $\propto \exp[T/(7\,\text{Gyr})]$ (Bovy 2017) is applied to the thin disk, while a mono-age of 12 Gyr for the thick disk and a Gaussian distribution of 9 ± 1 Gyr for the bar are respectively assumed. The IFMR is based on Raithel et al. (2018), who combined observational data of BHs and neutron stars with 1D neutrino-driven supernova simulations by Sukhbold et al. (2016).

In the IFMR, stars with initial masses of $15 < M_{\text{ini}}/M_\odot < 120$ probabilistically evolve into BHs with masses between $\sim 5 M_\odot$ and $\sim 16 M_\odot$ (see Figure 6 of Lam et al. 2020 for the IFMR for BHs). The probabilities of being a BH are $P_{\text{evo,BH}} = 0.321, 0.167,$ 0.500, 1.000, 0.348, 1.000, and 0.600 for initial mass ranges of 15–$17.8 M_\odot$, 17.8–$18.5 M_\odot$, 18.5–$21.7 M_\odot$, 21.7–$25.2 M_\odot$, 25.2–$27.5 M_\odot$, 27.5–$60 M_\odot$, and 60–$120 M_\odot$, respectively. The present-day mass function expects ~ 0.0035 BHs per main-sequence star in a typical line of sight toward the Galactic bulge.

2.2. BH Kick Velocity

In the original model by K21, a natal kick velocity of $100\,\text{km s}^{-1}$ in a random direction is added to the velocity of the BH progenitor following the prescription of Lam et al. (2020). In this paper, we consider five different values of the average kick velocity, $v_{\text{avg}} = 25, 50, 100, 200,$ and $400\,\text{km s}^{-1}$. The range of v_{avg} is broadly taken because there are no observations of the velocity of isolated BHs, except for OGLE-2011-BLG-0462/MOA-2011-BLG-191 (Lam et al. 2022; Sahu et al. 2022; Lam & Lu 2023), which has a transverse velocity of $37.6 \pm 5.1\,\text{km s}^{-1}$ (Lam & Lu 2023).

Also, instead of a fixed speed used in the original model, we consider a kick velocity that follows the Maxwell distribution

$$f(v_{\text{kick}}) = \frac{4\pi v_{\text{kick}}^2}{(2\pi\sigma_{\text{kick}}^2)^{3/2}} \exp\left(-\frac{v_{\text{kick}}^2}{2\sigma_{\text{kick}}^2}\right), \qquad (3)$$

where $\sigma_{\text{kick}}^2 = \pi\, v_{\text{avg}}^2/8$ is the 1D velocity dispersion, which is the same in the x, y, and z directions (i.e., $\sigma_{\text{kick}}^2 = \sigma_{x,\text{kick}}^2 = \sigma_{y,\text{kick}}^2 = \sigma_{z,\text{kick}}^2$), and v_{kick} is the magnitude of the 3D kick velocity. Note that Rose et al. (2022) showed that the t_E distribution of microlensing events due to BH lenses is insensitive to whether v_{kick} is given by a fixed value or by the Maxwell distribution with the same average value as the fixed value.

2.2.1. Scale Height of a BH Disk

Although not considered in K21 or Lam et al. (2020), the BH population should be in different states of dynamical equilibrium than the other stars because of the additional kick velocity. Tsuna et al. (2018) numerically evaluated this effect by calculating BHs' orbits in a potential that mimics our Galaxy as a function of average BH velocity, and we combined their results with K21's model.[7]

At first, we see how the scale height in the Tsuna et al. (2018) model depends on the radius from the Galactic center, R, and on the average velocity of the Maxwell distribution of the BH natal kick, v_{avg}. Here, the scale height in the Tsuna et al. (2018) model is defined by $h_{\text{T18}} \equiv \Sigma_{\text{T18}}/(2\rho_{\text{T18}})$, where Σ_{T18} is the surface density of the BH distribution in dynamical equilibrium, and ρ_{T18} is the volume density at the disk plane. Figure 1 shows the distribution of h_{T18} as a function of R and v_{avg}. We find that h_{T18} at $1.25 < R/\text{kpc} < 8.75$ is well explained by an analytic formula,

$$h_{\text{T18}} = 210\,\text{pc} \exp\left[\frac{R - R_\odot}{R_{\text{BH,0}}}\right] \left(\frac{v_{\text{avg}}}{25\,\text{km s}^{-1}}\right)^{\beta_{\text{BH}}}, \qquad (4)$$

where $R_{\text{BH,0}} = 9.66$ kpc, $\beta_{\text{BH}} = 0.82$, and $R_\odot$ is the distance to the Galactic center from the Sun and we use $R_\odot = 8.16$ kpc. The inner region of $R < 1$ kpc was not fitted by this formula, as shown in Figure 1. This is because the bulge stars, which have different distributions from disk stars, dominate the area. Here, we do not consider any modifications to the bulge density model and use the original model of K21 for simplicity. In Section 5.1.1, we apply a simple modification to the bulge density model to show that it does not change our discussion about constraints on the kick velocity. The following modifications are only for the disk density model.

The v_{avg} dependence of h_{T18} can be interpreted as due to the vertical velocity dispersion dependence of the scale height, which is well known for the stellar component (e.g., van der Kruit & Freeman 2011). We incorporate this effect in the disk

---

[7] Ideally, we should repeat such a calculation of orbits under a potential corresponding to the stellar density profile of the K21 model. However, it is difficult because the K21 model is not a self-consistent model in terms of dynamics. Keeping consistency with both dynamics and the data fitted in K21 requires a lot of effort and is beyond the scope of this paper. Nevertheless, combining the results of Tsuna et al. (2018) with the K21 model should be approximately valid because both models are supposed to reproduce our Galaxy.

model by K21 as

$$h_{\mathrm{BH},i} = h_{0,i}\, g(R) \left(\frac{\sigma_{z,i,\mathrm{BH}}(R)}{\sigma_{z,i}(R)} \right)^{\beta_{\mathrm{BH}}}, \qquad (5)$$

with the vertical velocity dispersion of BHs enhanced due to the kick,

$$\sigma_{z,i,\mathrm{BH}}(R) = \sqrt{\sigma_{z,i}(R)^2 + \pi\, v_{\mathrm{avg}}^2/8}, \qquad (6)$$

where i takes 1–8 to denote each of the seven thin disks with different ages ($i = 1, 2, \ldots\, 7$) and one thick disk ($i = 8$) in the K21 model, $h_{0,i}$ is the scale height of the ith disk that is given in Table 1 of K21 as $z_{\mathrm{d},\odot}$, and $\sigma_{z,i}(R)$ is the vertical velocity dispersion of stars in the ith disk, which is given by

$$\sigma_{z,i}(R) = \begin{cases} 24.4\ \mathrm{km\ s^{-1}} \left(\dfrac{T_i + T_{\min}}{T_{\max} + T_{\min}} \right)^{0.77} \exp\left[-\dfrac{R - R_\odot}{5.9\ \mathrm{kpc}} \right] & (i = 1, 2, \ldots 7) \\[12pt] 49.2\ \mathrm{km\ s^{-1}} \exp\left[-\dfrac{R - R_\odot}{9.4\ \mathrm{kpc}} \right] & (i = 8), \end{cases}$$

$$(7)$$

where $T_{\min} = 0.01$ Gyr, $T_{\max} = 10$ Gyr, and T_i is the mean age of the stars in the ith thin disk given by 0.08, 0.59, 1.52, 2.52, 4.07, 6.07, and 8.66 Gyr for $i = 1$ to 7, respectively, which reflects the assumed star formation rate for the thin disk of $\propto \exp[T/(7\ \mathrm{Gyr})]$ (Bovy 2017).

The remaining factor in Equation (5) not yet explained is $g(R)$. This is introduced to smoothly connect the h_{T18} formula depending on R by $\exp[(R - R_\odot)/R_{\mathrm{BH},0}]$ to the scale height of K21's disk model that is constant for R. The scale height in Tsuna et al. (2018), h_{T18}, increases with R because they assumed that BHs have a uniform velocity dispersion regardless of their positions, which results in a larger scale height at the outer part of the Galaxy where the gravity is weaker. On the other hand, K21 introduced a model for the velocity dispersion of stars that decreases with R, which is supported by the Gaia data (Gaia Collaboration et al. 2018). Therefore, we need a formula to give the scale height of BHs that bridges two regimes that have different R-dependence of the scale height: the regime where the stellar velocity dispersion $\sigma_{z,i}(R)$ is dominant and the regime where the kick velocity dispersion $\pi\, v_{\mathrm{avg}}^2/8$ is dominant. We use

$$g(R) = \exp\left[\frac{R - R_\odot}{R_{\mathrm{BH}}(R)} \right], \qquad (8)$$

where

$$R_{\mathrm{BH}}(R) = R_{\mathrm{BH},0} \left(1 + \frac{\sigma_{z,i}(R)^2}{\pi\, v_{\mathrm{avg}}^2/8} \right), \qquad (9)$$

to connect smoothly the regime of large kick velocity (i.e., $\pi v_{\mathrm{avg}}^2 \gg \sigma_{z,i}$) and that of small kick velocity (i.e., $\pi v_{\mathrm{avg}}^2 \ll \sigma_{z,i}$). Although this is a crude attempt to include a dependence on R, we show in Section 5.1.3 that our main results of the constraint on kick velocity are not affected by how this is connected.

Figure 2 shows the scale height for disk BHs (i.e., Equation (5)) as a function of the average kick velocity v_{avg} for each of the ith disk components at $R = R_\odot$. At the high end of v_{avg}, all the components have lost their original velocity dispersion information and have the same velocity dispersion due to the kick velocity. In such a region, a smaller i (younger)
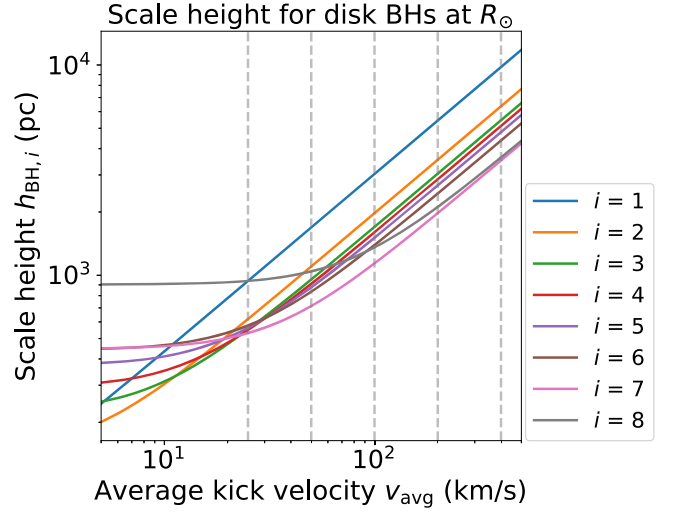

Figure 2. Our scale height model for disk BHs as a function of the average velocity of the Maxwell distribution of the BH natal kick. Different colors indicate different disk components ($i = 1$–7 for thin disk and $i = 8$ for thick disk). Five vertical dashed gray lines indicate the considered v_{avg} values (25 km s^{-1}, 50 km s^{-1}, 100 km s^{-1}, 200 km s^{-1}, and 400 km s^{-1}) in this paper.
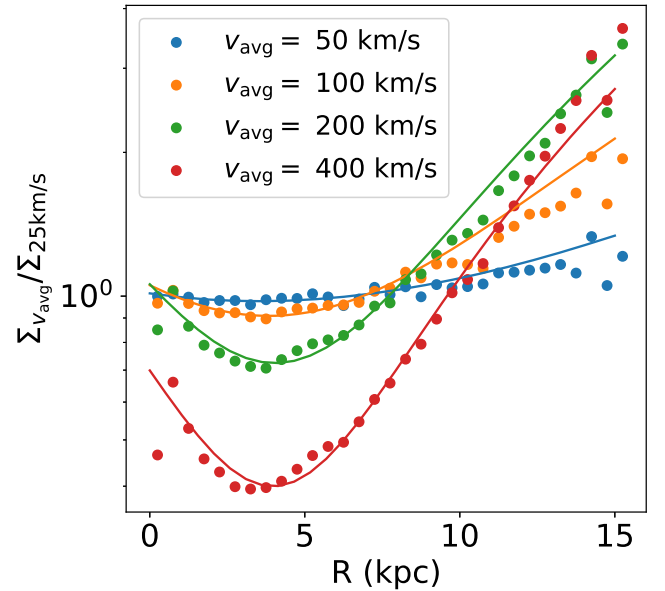

Figure 3. Dots show the surface density with $v_{\mathrm{avg}} = 50$, 100, 200, and 400 km s^{-1} as a function of R relative to the one with $v_{\mathrm{avg}} = 25$ km s^{-1} from the numerical model by Tsuna et al. (2018). The solid lines show the second-order polynomial curves fitted to each of the three in $0.75 < R/\mathrm{kpc} < 8.25$.

component has a larger scale height because its surface density is less massive than older component disks, and therefore its gravity is smaller.

2.2.2. Surface Density of a BH Disk

In addition to the scale height dependence on the kick velocity, the numerical model by Tsuna et al. (2018) also shows the dependence of the surface density on the kick velocity. Dots in Figure 3 show the surface density in the numerical models by Tsuna et al. (2018) for $v_{\mathrm{avg}} = 50$, 100, 200, and 400 km s^{-1} relative to the one with $v_{\mathrm{avg}} = 25$ km s^{-1}. We found that a second-order polynomial curve (shown in Figure 3) can well fit each of the relative surface densities.

Table 1
Comparison of Properties between Stars and BHs

Property	Location	Stars	BHs	Refer to
Velocity	Disk and bulge	$\boldsymbol{v}$	$\boldsymbol{v} + \boldsymbol{v}_{\text{kick}}$	Equation (3)
Scale height	Disk	$h_{0,i}$	$h_{0,i}\, g(R)\left(\frac{\sigma_{z,i,\text{BH}}(R)}{\sigma_{z,i}(R)}\right)^{\beta_{\text{BH}}}$	Equation (5)
Surface density	Disk	$\Sigma_0(R)$	$\Sigma_0(R)\, \eta(R; v_{\text{avg}})$	Equation (10)

Thus, we use

$$\Sigma_{\text{BH}}(R; v_{\text{avg}}) = \Sigma_0(R)\, \eta(R; v_{\text{avg}}), \tag{10}$$

with $\eta(R; v_{\text{avg}}) = a + b\,(R/\text{kpc}) + c\,(R/\text{kpc})^2$ for the surface density of the BH population with the average kick velocity of v_{avg}. Here, $\Sigma_0(R)$ is the original surface density of the K21 model and we determined the coefficients a, b, and c in $\eta(R; v_{\text{avg}})$ based on Figure 3; $(a,\ b,\ c) = (1, 0, 0)$, $(1.013, -0.020, 0.003)$, $(1.054, -0.075, 0.010)$, $(1.059, -0.166, 0.021)$ and $(0.699, -0.151, 0.019)$ for $v_{\text{avg}} = 25$, 50, 100, 200, and 400 km s^{-1}, respectively.

All modifications applied to the BH population described in this section are summarized in Table 1.

3. Influence on Microlensing Distributions

As described in Section 1, the Einstein radius crossing time t_{E} and the microlens parallax π_{E} are the two common microlens parameters that are constrained in the case of BH candidate events. Because $t_{\text{E}} \propto \sqrt{M_L}$, BH events tend to have large values of t_{E}. The microlens parallax π_{E} can be relatively easily measured in such a long-timescale event through the microlens parallax effect due to the Earth's orbital motion, although there is another drawback that a massive lens like BHs will have a smaller π_{E}, making it more difficult to measure.

Here, we consider the influence of changing kick velocity on the t_{E} distribution and the two-dimensional distribution of t_{E} and π_{E}. In this work, we use a modified version of genulens (Koshimoto & Ranc 2022) to simulate microlensing events following the model described in Section 2. Note that we simulate the distribution of t_{E} in the heliocentric frame (i.e., with Earth's velocity projected on the sky, $v_{\oplus,\perp} = 0$) for simplicity, although t_{E} is normally measured in the geocentric frame. To validate our results, we repeated the calculations presented below with $v_{\oplus,\perp}(l,\ b) = (11.2,\ -22.9)$ km s^{-1} and confirmed similar results (e.g., the Γ_{BH} values presented in Table 2 changed less than 10%), where the applied projected Earth velocity value is for June, middle of the bulge season.

3.1. Event Rate as a Function of t_E

3.1.1. Influence on Disk BH Event Rate

Figure 4 shows the t_{E} distribution of BH lens events as a function of the average kick velocity v_{avg}. We use a Monte Carlo simulation of 3×10^7 realizations of microlensing events toward $(l, b) = (-0.14, -1.62)$, i.e., the event coordinate of the isolated stellar-mass BH event OGLE-2011-BLG-0462/MOA-2011-BLG-191 (hereafter OB110462, Lam et al. 2022; Sahu et al. 2022), and Figure 4 shows the fraction of disk BH events out of all simulated events. In each v_{avg} panel, the blue histogram shows the distribution when the kick velocity is

added to the BH velocities but the scale height or the surface density does not change (same as the treatment by previous studies such as that of Lam et al. 2020 or K21). The orange histogram shows the distribution when the scale height and the surface density are also modified according to the added kick velocity.

Because $t_{\text{E}} \propto \mu_{\text{rel}}^{-1}$, t_{E} gets shorter as v_{avg} gets faster. This generally results in a higher event rate because the microlensing event rate is proportional to $\mu_{\text{rel}}\theta_{\text{E}}$, the area of the sky swept by the Einstein ring of an event per unit time. This is why the blue histogram shows a higher event fraction with faster v_{avg}. On the other hand, the orange histogram shows the opposite trend in terms of the event rate compared to the blue histogram, although the shape of the t_{E} distribution itself is similar. The difference between the blue and orange histograms in the event fraction is larger when v_{avg} is faster. The difference is relatively small when $v_{\text{avg}} \leqslant 100$ km s^{-1} because the additional velocity due to the kick is yet comparable to the progenitors' original velocity, whereas it gets more prominent at $v_{\text{avg}} \geqslant 200$ km s^{-1}. It predicts two times fewer BH events at $v_{\text{avg}} = 200$ km s^{-1} and approximately 6 times fewer BH events at $v_{\text{avg}} = 400$ km s^{-1} when we consider the inflation of the BH disk due to the kick velocity. This is because the BH disk becomes thicker with a faster kick velocity as shown in Figure 2, and its abundance at a low-latitude field (e.g., toward the Galactic bulge) becomes relatively less dominant. Therefore, we would end up overestimating the BH event fraction, especially when the kick velocity is fast, unless we properly consider the scale height inflation due to the kick.

3.1.2. Comparison with the OGLE-IV t_E Distribution

Mróz et al. (2017) analyzed microlensing events discovered in the OGLE-IV high-cadence fields between 2010 and 2015, while Mróz et al. (2019) analyzed microlensing events in the OGLE-IV low-cadence fields between 2010 and 2017. They provided t_{E} distributions and detection efficiencies (P. Mróz, private communication) in both fields.

Figure 5 shows the comparison of the OGLE-IV t_{E} distributions with the model distributions calculated with different average kick velocity v_{avg}. With each v_{avg} value, we performed a Monte Carlo simulation to have a model t_{E} distribution in the OGLE-IV survey fields. We then multiplied the detection efficiency by the model t_{E} distribution, and we normalized the distribution by the total number of OGLE-IV events detected to have the blue dashed curves, $\Gamma_{\text{all}}(t_{\text{E}})\, \epsilon\, (t_{\text{E}})$, in Figure 5 (see Section 4.1.5 of K21 for more details of this calculation). In this way, the original model t_{E} distribution, shown in blue solid curves, is also normalized.

Figure 5 shows that the observed distribution (gray histograms) can be well reproduced by the model event rate multiplied by the detection efficiency (blue dashed curve) regardless of the v_{avg} value. This indicates all the considered v_{avg} values are acceptable in terms of consistency with the OGLE t_{E} distribution. However, we know that there is one BH event, OB110462 (Lam et al. 2022; Sahu et al. 2022), that occurred during the OGLE-IV survey period analyzed by the Mróz et al. papers shown as red dotted lines. This fact enables us to constrain the kick velocity, as discussed in detail in Section 4.

Table 2
Estimated Number of BH Events like OGLE-2011-BLG-0462 That Occurred during the OGLE-IV Survey by Mróz et al. (2017, 2019)

Model[a]	Average Kick Velocity v_{avg}				
	25 km s^{-1}	50 km s^{-1}	100 km s^{-1}	200 km s^{-1}	400 km s^{-1}
	$N_{exp,0462}$ ($\Gamma_{BH} P_{BH}$)	$N_{exp,0462}$ ($\Gamma_{BH} P_{BH}$)	$N_{exp,0462}$ ($\Gamma_{BH} P_{BH}$)	$N_{exp,0462}$ ($\Gamma_{BH} P_{BH}$)	$N_{exp,0462}$ ($\Gamma_{BH} P_{BH}$)
Fiducial	0.52 (4.9 0.11)	**0.38** (4.4 0.087)	**0.18** (3.4 0.053)	**0.042** (1.9 0.022)	**0.0040** (0.63 0.0063)
Inflate-bar	**0.51** (4.8 0.11)	**0.38** (4.4 0.088)	**0.18** (3.3 0.056)	**0.044** (1.6 0.027)	**0.0042** (0.29 0.014)
Özel–MF	**0.59** (3.7 0.16)	**0.44** (3.4 0.13)	**0.19** (2.4 0.081)	**0.040** (1.2 0.034)	**0.0037** (0.38 0.0098)
$P_{evo,BH} = 1$	**0.92** (5.7 0.16)	**0.66** (5.0 0.13)	**0.31** (3.8 0.081)	**0.067** (2.0 0.034)	**0.0062** (0.62 0.010)
$R_{BH} = R_{BH,0}$	**0.49** (5.0 0.11)	**0.33** (4.5 0.088)	**0.16** (3.5 0.053)	**0.038** (1.9 0.022)	**0.0036** (0.63 0.0063)
$R_{BH} = \infty$	**0.48** (4.7 0.10)	**0.34** (4.2 0.083)	**0.15** (3.2 0.049)	**0.035** (1.7 0.020)	**0.0035** (0.64 0.0054)

Notes. Γ_{BH} refers to $\Gamma_{BH}(u_0 < 0.1, t_E > 200$ days), P_{BH} refers to $P_{BH}(\pi_E > 0.06 \mid t_{E,OB110462})$, and $N_{exp,0462}$ refers to the expected number of both happening, which is shown in bold font.
[a] Fiducial model, described in Section 2, uses the Lam et al. (2020)'s BH IFMR and considers the disk scale height inflation due to the natal kick. The inflate-bar model is the fiducial model but with a bar scale height inflation due to the natal kick. The Özel–MF model is the fiducial model but uses Özel et al. (2010)'s Gaussian BH IFMR. $P_{evo,BH} = 1$ model is the Özel–MF model but with $P_{evo,BH} = 1$ for the probability of evolving into BHs for stars with $M_{ini} > 15 \, M_\odot$. The $R_{BH} = R_{BH,0}$ model is the fiducial model but uses $R_{BH} = R_{BH,0}$ in Equation (9). The $R_{BH} = \infty$ model is the fiducial model but uses $R_{BH} = \infty$ in Equation (9), i.e., uses $g(R) = 1$.

3.2. Distribution of t_E versus π_E

A similar approach can be done on the t_E versus π_E plane. Lam et al. (2020) showed that ~85% of the lenses are due to BHs in events with $t_E > 120$ days and $\pi_E < 0.08$ when the kick velocity is 100 km s^{-1} for BHs. This is also confirmed with our model as shown in the $v_{avg} = 100$ km s^{-1} panel in Figure 6, where the cyan dashed lines indicate the region of $t_E > 120$ days and $\pi_E < 0.08$. The figure also shows the same distribution with different v_{avg} values. This indicates that the t_E distributions of the BH population are similar in $v_{avg} = 25, 50,$ and 100 km s^{-1}, but the distribution shifts to the shorter t_E side as v_{avg} exceeds 100 km s^{-1}. This is because the additional kick velocity becomes more dominant than the original celestial velocity at $v_{avg} > 100$ km s^{-1}.

The BH population (black dots) is not distributed around the (t_E, π_E) value observed for OB110462 when $v_{avg} = 200$ km s^{-1} and 400 km s^{-1}, which implies these high kick velocity values are unlikely. The rare position of OB110462 among the black dots is due to its close distance from the Sun of $D_L = 1.72^{+0.32}_{-0.23}$ kpc (Lam & Lu 2023), significantly closer than the typical ($\sim2\,\sigma$) range of D_L for BH lenses in our model of ~3 to ~9 kpc. We further discuss this event in Section 4.

4. Implication of Average Kick Velocity from OGLE-2011-BLG-0462

The only unambiguous isolated BH event to date, OGLE-2011-BLG-0462/MOA-2011-BLG-191 (OB110462), resides in so unique parameter space ($t_E = 276 \pm 6$ days in the heliocentric frame, $u_0 = 0.05 \pm 0.01$, $\pi_E = 0.10 \pm 0.01$; Lam & Lu 2023) that this single event can be used to obtain some restrictions on the kick velocity. Lam & Lu (2023) also pointed out the rareness of this event but concluded that understanding the selection effect is needed for further discussion. Indeed, the

selection effect is not well understood for this event. Nevertheless, in this section, we attempt to compare the number of BH events expected by a model with the actual number under some plausible assumptions.

The lens object of OB110462 was identified as a BH thanks to the astrometric microlensing measurements using Hubble Space Telescope (HST) data (Lam et al. 2022; Mróz et al. 2022; Sahu et al. 2022; Lam & Lu 2023). The HST data were observed in a series of HST follow-up programs by Sahu et al. that aimed to discover the first isolated stellar-mass BH via astrometric microlensing. The HST programs monitored five events selected from those alerted between 2009 and 2011 by the OGLE[8] and MOA[9] alerting systems with $t_E > 200$ days and high magnifications (Sahu 2009; Lam et al. 2022). The actual size of the total sample that Sahu et al. (2009, 2011, 2012) looked at to select the five events is unknown, but it may be assumed to be smaller than the total events alerted from 2009–2011.

On the other hand, the OGLE-IV sample plotted in Figure 5 was systematically selected from the OGLE-IV high-cadence fields between 2010 and 2015 by Mróz et al. (2017) and from the OGLE-IV low-cadence fields between 2010 and 2017 by Mróz et al. (2019). The combined sample covers the entire OGLE-IV bulge fields for 6 yr, and the sample size should be larger than the one that Sahu et al. (2022) looked at. Thus, we here consider how many BH events are expected in the OGLE-IV sample by Mróz et al. (2017, 2019) with $u_0 < 0.1$ and $t_E > 200$ days and compare the number with the actual number, at least one. The range $u_0 < 0.1$ is determined to meet the requirement of high magnifications in the event selection by the HST programs. The interpretation of "high magnifications" is
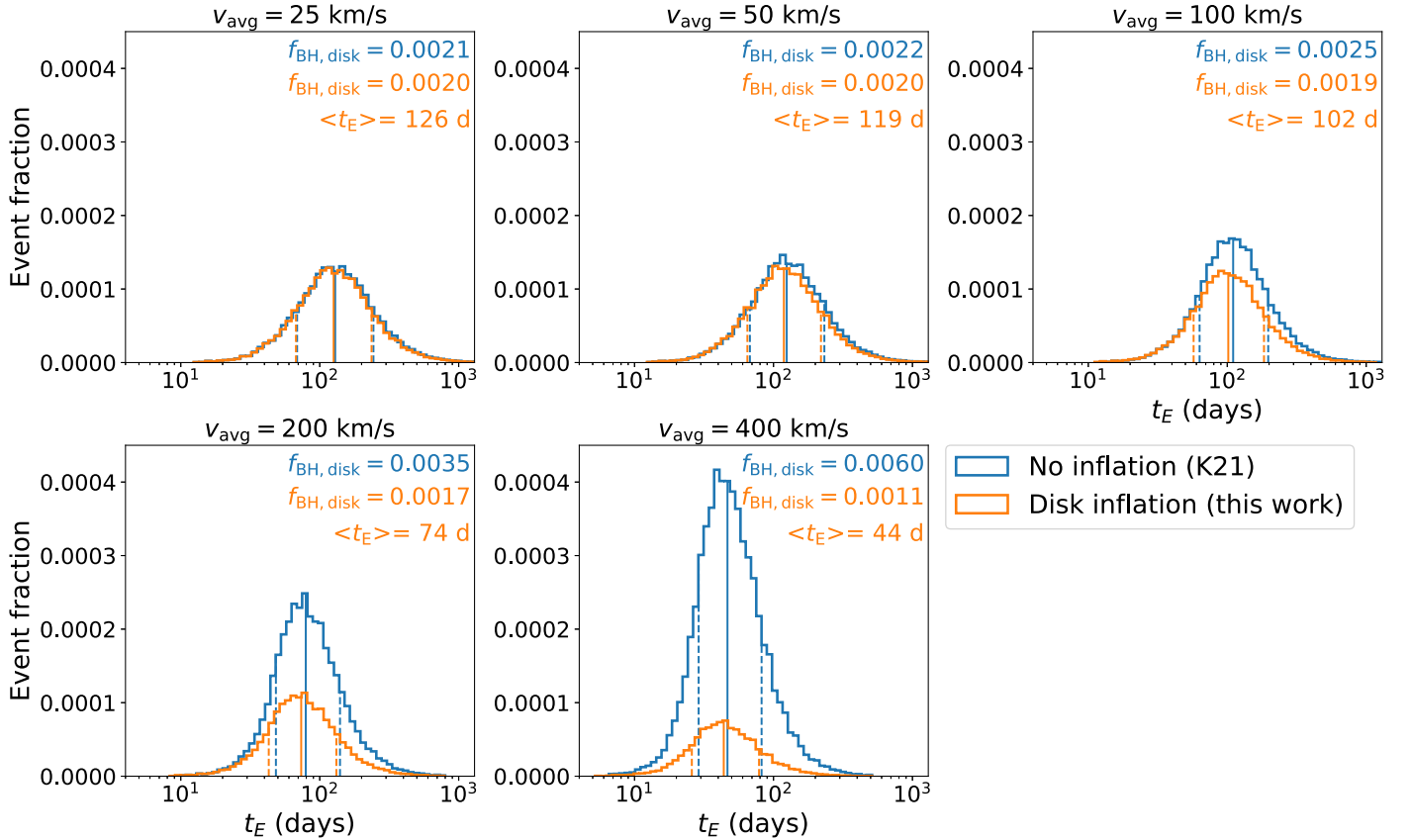
---

[8] https://ogle.astrouw.edu.pl/ogle4/ews/ews.html
[9] https://www.massey.ac.nz/~iabond/moa/alerts/

Disk BH event t_E distributions with various average kick velocity v_{avg}

Figure 4. Event fraction of disk BH events as a function of t_E for different average kick velocity v_{avg}. The event fraction is relative to all the simulated 3×10^7 microlensing events toward $(l, b) = (-0.14, -1.62)$, the event coordinate of the isolated stellar-mass BH event OGLE-2011-BLG-0462/MOA-2011-BLG-191.

somewhat arbitrary, and we have conservatively taken $u_0 < 0.1$ (corresponding to peak magnification $\gtrsim 10$), not to underestimate the expected numbers calculated below and avoid constraining v_{avg} too much. The cut with $t_E > 200$ days is not best to reproduce the event selection by Sahu et al. because they presumably selected the samples for HST observations when some of the events were still ongoing and the t_E measurements were not yet finalized. In fact, four out of the five events from the HST program have t_E less than 200 days, according to Lam et al. (2022). We will discuss the influence of changing this criterion in Section 5.2.

An issue in the comparison is that the BH event OB110462 did not pass the selection criteria by Mróz et al. (2017) due to its too-bright blending flux (P. Mróz, private communication), meaning that the BH event was not "detected" by their criteria and did not remain in the final statistical sample. Therefore, the statement that there is at least one BH event in the sample is not true if we consider only the "detected" events. To include OB110462, we consider the number of events "occurring" during the survey instead of the number of events "detected." This can be calculated by dividing the number of detected events, $\epsilon \Gamma_{all}$ shown in the blue dashed curves in Figure 5, by the detection efficiency of the OGLE-IV survey, ϵ. The blue solid curve in each panel of Figure 5 shows the t_E distribution of the number of events "occurring" during the survey, Γ_{all}. The detection efficiency was calculated by injection and recovery tests of artificial events with $0 < u_0 < 1.5$ and $I_S < 22$ by Mróz et al. (2017) and with $0 < u_0 < 1.0$ and

$I_S < 21$ by Mróz et al. (2019). Thus, Γ_{all} in the top panels of Figure 5 represents all events occurring with $0 < u_0 < 1.5$ and $I_S < 22$ in the OGLE-IV high-cadence fields between 2010 and 2015, while Γ_{all} in the bottom panels represents all events occurring with $0 < u_0 < 1.0$ and $I_S < 21$ in the OGLE-IV low-cadence fields between 2010 and 2017. OB110462 has $u_0 = 0.05 \pm 0.01$ (Lam & Lu 2023) and $I_S = 19.8$ mag (Mróz et al. 2022) and is supposed to be included in Γ_{all} for the high-cadence fields.

The orange solid curves in Figure 5 show subsamples of Γ_{all} for BH events with $u_0 < 0.1$, $\Gamma_{BH}(u_0 < 0.1)$. The sums of the expected numbers of BH events with $t_E > 200$ days in both high-cadence and low-cadence fields are $\Gamma_{BH}(u_0 < 0.1, t_E > 200 \text{ days}) = 4.9, 4.4, 3.4, 1.9,$ and 0.63 for $v_{avg} = 25, 50, 100, 200,$ and 400 km s^{-1}, which are also shown in the fiducial model line in Table 2 as Γ_{BH}. The $\Gamma_{BH}(u_0 < 0.1, t_E > 200 \text{ days})$ values are less than 1 for $v_{avg} = 400$ km s^{-1}, suggesting that such fast v_{avg} might be unlikely when compared with the actual number of events occurring, at least one. Nevertheless, this alone does not put an effective constraint on the average speed because the Poisson probabilities of having more than one event are $0.993, 0.988, 0.967, 0.850,$ and 0.467 for $v_{avg} = 25, 50, 100, 200,$ and 400 km s^{-1}, respectively, which all are reasonable probabilities to happen.

However, as discussed in Section 3.2, OB110462 has a unique π_E value among the BH events with t_E values similar to OB110462, especially for high v_{avg} values (see Figure 6). To further constrain v_{avg}, we consider the probability of having such
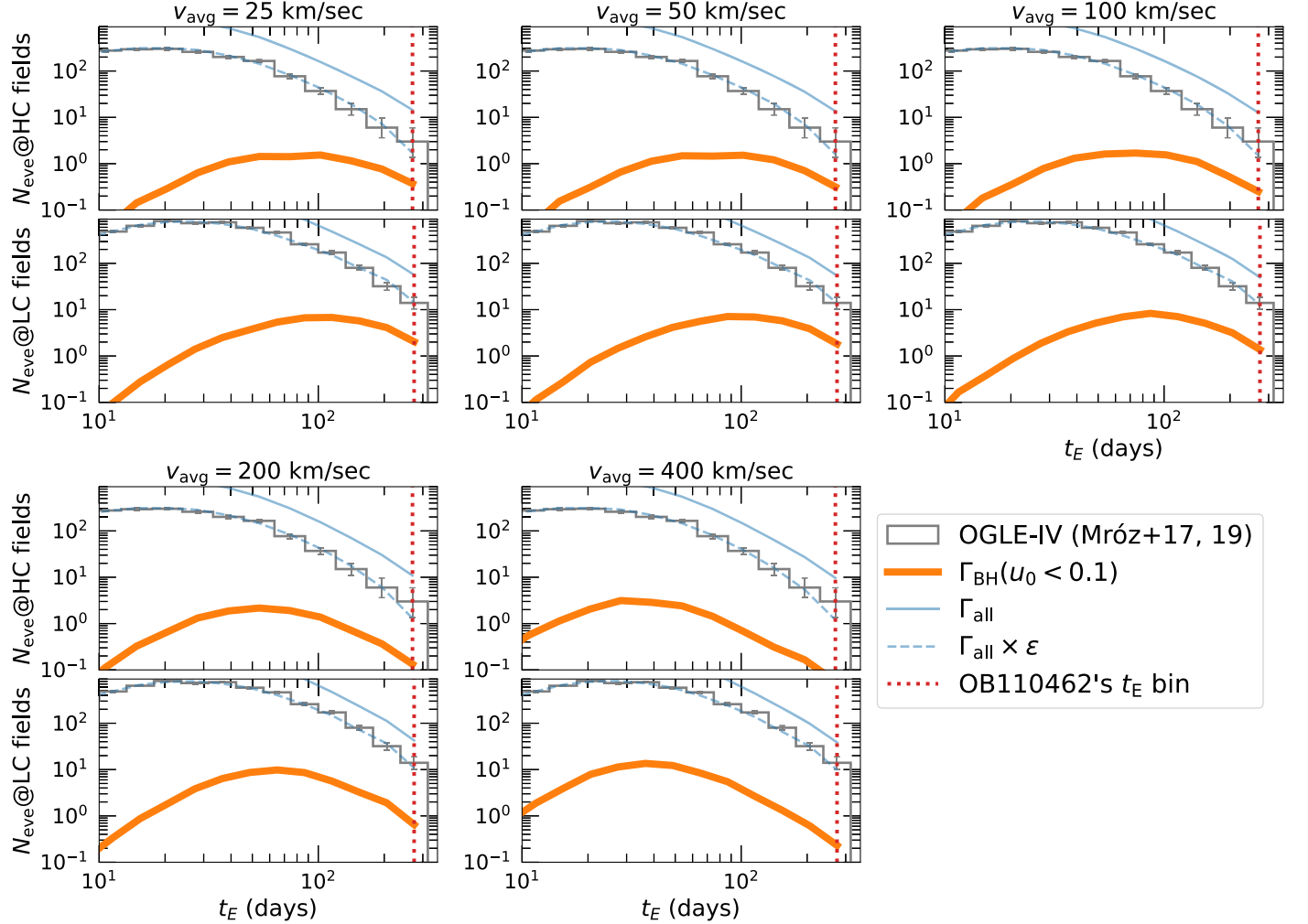
Comparison with OGLE-IV t_E distribution

Figure 5. Observational t_E distributions in the OGLE-IV high-cadence (top of each panel, Mróz et al. 2017) and low-cadence (bottom of each panel, Mróz et al. 2019) fields compared with model event rate calculated for different average kick velocity v_{avg}. The dashed blue line shows the event rate multiplied by the OGLE-IV detection efficiency, which fits the observational distributions well. The solid blue line shows the event rate before multiplying the detection efficiency, corresponding to the number of events occurring during the OGLE-IV survey. The solid orange line shows that of BH lenses but for $u_0 < 0.1$.

a rare π_E value when we randomly pick one BH event that has $u_0 < 0.1$ and $t_E > 200$ days. Figure 7 shows the probability distribution of π_E for BH lens events with $270 < t_E/\mathrm{days} < 282$ (1σ uncertainty region of t_E for OB110462) for different v_{avg} values. The vertical red lines indicate the median and 3σ range of π_E of OB110462 estimated by Lam & Lu (2023), where we take the 3σ range ($0.06 < \pi_E < 0.14$) from their Figure 15. As seen in the top panel of Figure 7, the probabilities of π_E larger than the 3σ lower limit value are $P_{BH}(\pi_E > 0.06 \,|\, t_{E,OB110462}) = 0.11$, 0.087, 0.053, 0.022, and 6.3×10^{-3} for $v_{avg} = 25, 50, 100, 200$, and 400 km s^{-1}, respectively. When multiplying by $\Gamma_{BH}(u_0 < 0.1, t_E > 200$ days), we have $N_{exp,0462} = 0.52, 0.38, 0.18, 0.042$, and 4.0×10^{-3} for $v_{avg} = 25, 50, 100, 200$, and 400 km s^{-1}, respectively. Here, $N_{exp,0462}$ represents the expected number of BH events occurring with $u_0 < 0.1$, $t_E > 200$ days, and π_E values as rare as OB110462 during the OGLE-IV survey. Hereafter, we shortly refer to $N_{exp,0462}$ as the expected number of BH events like OB110462.

The $N_{exp,0462}$ values indicate that the average kick velocity is likely to be $v_{avg} \lesssim 100$ km s^{-1} and fast average kick velocity values like 200 km s^{-1} or 400 km s^{-1} are unlikely. We would

like to emphasize that our claim that such fast v_{avg} is unlikely is solely based on statistics using event rates, and is not directly based on a small transverse velocity of $v_{T,L} = 37.6 \pm 5.1$ km s^{-1} (Lam & Lu 2023) for the BH lens of OB110462.

5. Discussion

5.1. Model Uncertainty

Our estimate of the $N_{exp,0462}$ values in Section 4 may depend on the Galactic model used. There should be no major problems with the stellar distribution in our model because the K21 model is fitted to the stellar distribution toward the Galactic bulge. However, there are some uncertainties about the parameter distributions of BHs.

The microlensing event rate is a function of number density along the line of sight, the velocity distribution, and the mass distribution of lens objects. Among these, we have been considering various velocity distributions by changing average kick velocity values and their influences on the number density distribution of the disk BH. However, we have so far assumed that the bulge BH profile does not change by the additional
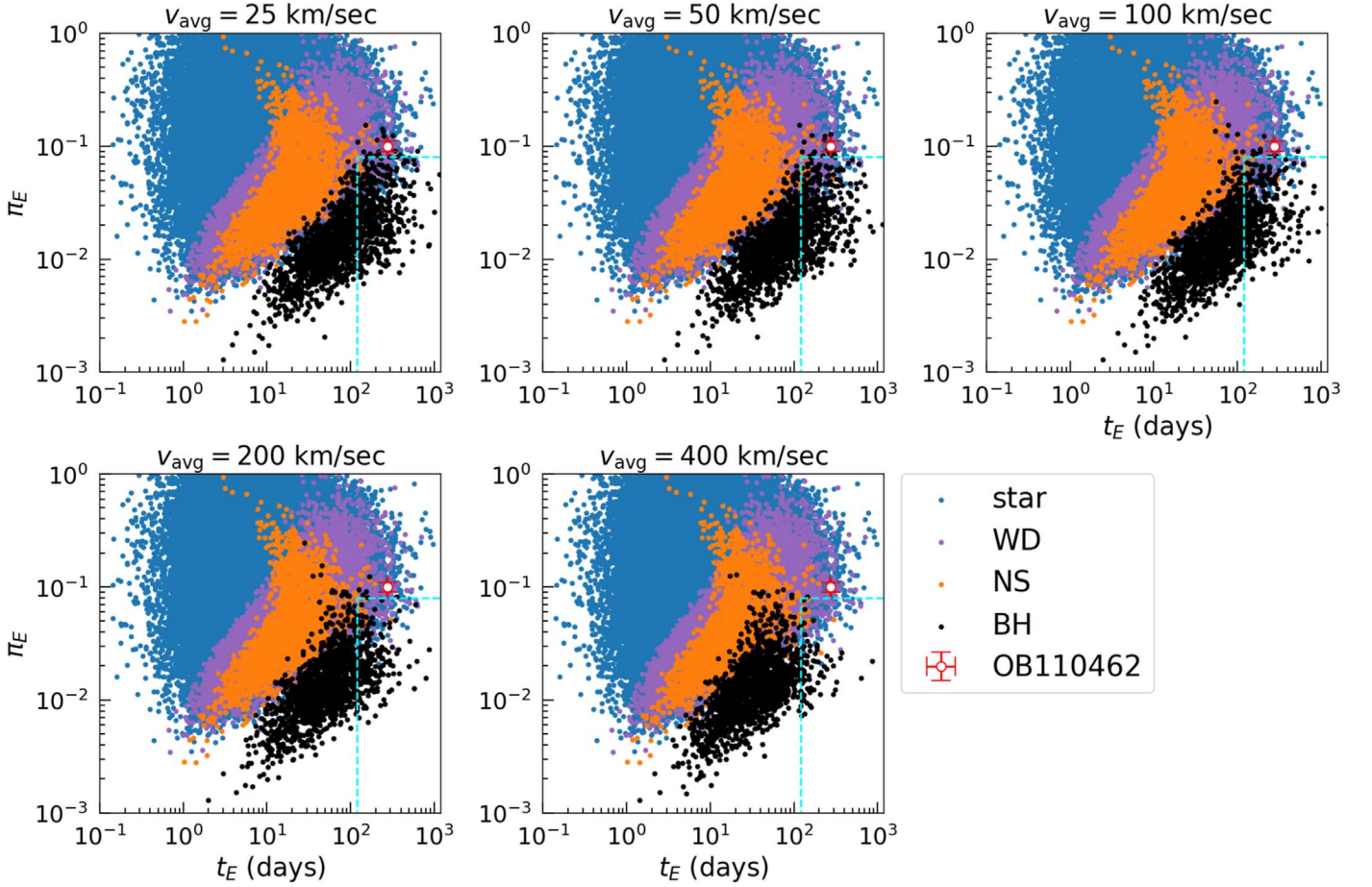
Figure 6. t_E vs. π_E distribution of 2×10^5 events randomly generated following our Galactic model with $v_{avg} = 25$, 50, 100, 200, and 400 km s^{-1}. The cyan dashed lines indicate the region of $t_E > 120$ days and $\pi_E < 0.08$ suggested by Lam et al. (2020) as a selection criterion for BH events. Note that Lam et al. (2020) applied a single BH kick velocity of 100 km s^{-1}.

kick velocity for simplicity. We have also fixed the BH mass distribution, which is another uncertain factor. Here we estimate how much these uncertainties affect our estimation of $N_{exp,0462}$, the expected number of BH lens events like OB110462 during the OGLE-IV survey by Mróz et al. (2017) and Mróz et al. (2019). The considered models and corresponding $N_{exp,0462}$ values are summarized in Table 2.

5.1.1. Density Distribution of Bulge BHs

As described in Section 2, we have not been considering the influence of the kick velocity on the bulge BH density distribution because modeling it requires a dynamical simulation under the potential created by the K21 model that is beyond the scope of this study. Nevertheless, here we consider how much this uncertainty likely affects our estimation of $N_{exp,0462}$. Figure 1 shows that the additional velocity inflates the scale height even in the bulge dominant region of $R \lesssim 1$ kpc. To qualitatively see the inflation effect, we apply Equation (5) but without $g(R)$, i.e.,

$$h_{BH,b} = h_{0,b} \left(\frac{\sqrt{\sigma_{z,b}(x', y', z)^2 + \pi \, v_{avg}^2/8}}{\sigma_{z,b}(x', y', z)} \right)^{\beta_{BH}}, \quad (11)$$

and use $h_{BH,b}$ as the scale height of the bar, corresponding to z_0 of the K21 bulge density model. Here, $h_{0,b} = 0.24$ kpc is the original scale height of the K21 bulge density model and

$\sigma_{z,b}(x', y', z)$ is the velocity dispersion of the bulge stars at (x', y', z) and given by Equation (19) of K21, where x' and y' are the positions along the major and minor axes of the bar, respectively.

We repeat the calculation of the expected number of BH events like OB110462 and the inflate-bar model lines of Table 2 show the results. When the bulge scale height is more inflated by the kick, the event rate of bulge lens events in the direction of OB110462, i.e., $(l, b) = (-0.14, -1.62)$, becomes lower. This leads to the smaller total event rates of BH events with $u_0 < 0.1$ and $t_E > 200$ days, $\Gamma_{BH}(u_0 < 0.1$, and $t_E > 200$ days, compared to the fiducial model (shown in Table 2). On the other hand, the decrease in bulge lenses leads to a relative increase in disk lenses, i.e., closer D_L, and since $\pi_E \propto \sqrt{D_L^{-1} - D_S^{-1}}$, π_E values also increase on average. This results in a higher probability of $P_{BH}(\pi_E > 0.06 \,|\, t_{E,OB110462})$ than the fiducial model. The lower probability of $t_E > 200$ days and the higher probability of $\pi_E > 0.06$ are canceled out when multiplied, resulting in almost the same expected number of BH events like OB110462 as the fiducial model, as shown in Table 2.

Since the same logic holds whether the density of the bulge BHs increases or decreases due to the natal kick, our estimate of the expected number of BH events is robust to the ignored effect of kick velocity on the density distribution of the bulge BHs.
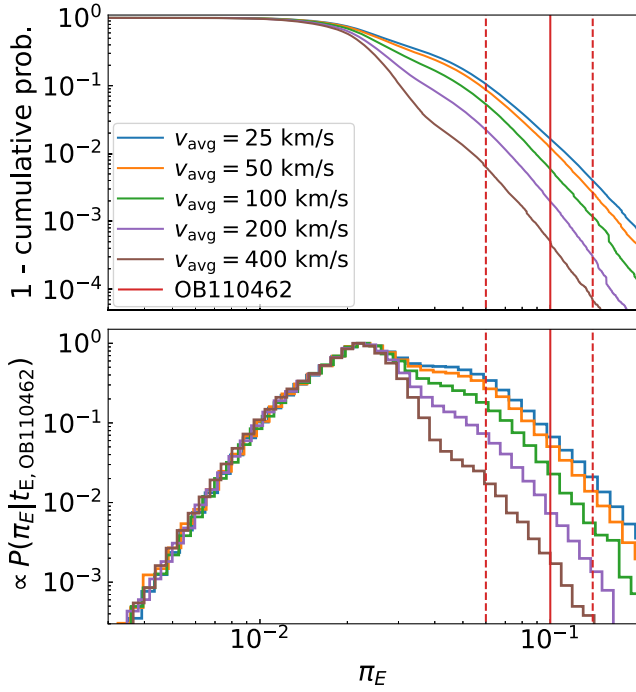
Figure 7. Cumulative probability (top) and relative probability (bottom) distributions of π_E for BH lens events with $270 < t_E$ days$^{-1} < 282$ (1 σ uncertainty region of t_E for OB110462) when v_{avg} is 25, 50, 100, 200, and 400 km s^{-1}. The relative probabilities in the bottom panel are normalized by the peak probability of each. The vertical red lines are the median (solid line) and the 3σ range (dashed lines) of π_E of OB110462 estimated by Lam & Lu (2023).

5.1.2. BH Mass Function

As described in Section 2, we have used Lam et al. (2020)'s probabilistic IFMR to calculate the present-day mass function for BHs, which is shown as a blue line in Figure 8. Another BH mass function often used is the Gaussian distribution of $7.8 \pm 1.2 \, M_\odot$ by Özel et al. (2010). The orange line in Figure 8 shows the BH mass distribution when we adopt the Gaussian distribution of $7.8 \pm 1.2 \, M_\odot$ as the BH IFMR instead of the Lam et al. (2020) IFMR but holds the same probabilities of evolving into a BH, $P_{evo,BH}$. Because the latest estimated mass for the BH lens of OB110462 by Lam & Lu (2023), $6.0^{+1.2}_{-1.0} \, M_\odot$, well overlaps the Özel et al. (2010)'s Gaussian distribution, a naive expectation is that the expected BH numbers calculated in Section 4 would increase if we adopt the Özel et al. (2010)'s BH mass function.

The Özel–mass function (MF) model line in Table 2 shows the recalculated expected number of BH events like OB110462. Contrary to the naive expectation above, the event rate of BH events with $u_0 < 0.1$ and $t_E > 200$ days, $\Gamma_{BH}(u_0 < 0.1, t_E > 200 \text{ days})$, for the Özel–MF model is lower than that for the fiducial model. This is because Lam et al. (2020)'s IFMR used in the fiducial model generates more massive BHs than Özel et al. (2010)'s IFMR, and generates more events with $t_E > 200$ days. Meanwhile, this in turn indicates that BH lens masses with the Özel–MF model are lower than those in the fiducial model on average, leading to higher values of π_E since $\pi_E \propto M_L^{-1/2}$. This results in a higher probability of $P_{BH}(\pi_E > 0.06 \,|\, t_{E,OB110462})$ for the Özel–MF model than the fiducial model. Similarly to the case of the inflate-bar model in Section 5.1.1, these two factors of the lower event rate and higher probability are canceled when
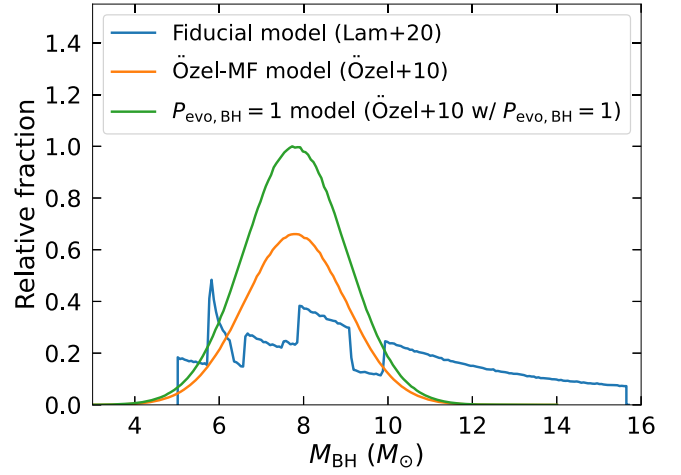

Figure 8. Comparison of BH mass functions used in the three different models in Table 2.

multiplied. This again leads to almost the same expected number of BH events like OB110462 for the Özel–MF model as those for the fiducial and inflate-bar models, as shown in Table 2. Since the same cancellation happens for any IFMR as long as the total number of BHs is the same, our estimate of the expected number of BH events is again robust to the shape of the BH mass function.

The above modification kept the fraction of stars that evolve into BHs, $P_{evo,BH}$, as a function of the initial mass range that is described in Section 2.1. However, even when we apply $P_{evo,BH} = 1$ for all stars with initial masses $> 15 \, M_\odot$, the number of BHs in the Galactic model only increases to 0.0054 BHs per main-sequence star from the original value of 0.0035 BHs per main-sequence star (see the green line in Figure 8). Although this leads to a factor of ~ 1.5 increase in the expected BH events, as shown in Table 2 as $P_{evo,BH} = 1$ model, it does not change our conclusion that $v_{avg} \geqslant 200$ km s^{-1} is unlikely.

5.1.3. Uncertainty in g(R)

We have been using Equation (5) for the disk BH scale height model, which includes an uncertain factor $g(R)$ to connect the two extremes of the disk models; one with a constant scale height but with a velocity dispersion dependent on R (when $v_{avg} = 0$), and the other with a scale height dependent on R but with a constant velocity dispersion (when $v_{avg} \to \infty$). How to connect these two extreme cases is uncertain, and we have been applying Equations (8) and (9). To estimate the possible variation of the expected number of BH events due to this uncertainty, we calculate $N_{exp,0462}$ with the two extreme cases. The $R_{BH} = R_{BH,0}$ and $R_{BH} \to \infty$ models in Table 2 show the results, and we confirm that our conclusion does not change due to this uncertainty.

5.1.4. Possibility of a Binary BH

Mróz et al. (2017) and Mróz et al. (2019) removed obvious binary lens events from their sample, and therefore, the t_E distribution shown in Figure 5 is for events with the shape of a single-lens event. However, the sample may still contain very close binary lenses because it is difficult to recognize a binary signal if the size of the central caustic made by the close binary is smaller than u_0.

Because our model has been only considering single BHs, including such unrecognized binary BHs could increase the expected number of BH events. Assuming each component of binary BHs follows the same BH mass function as what we considered for single BHs, an equal-mass binary BH system will have its system mass function that doubles the mass of the mass function for single BHs. Therefore, events with $t_E \gtrsim 140$ days in a single BH-only model could potentially contribute $t_E > 200$ days when we consider a model with binary BH population.

However, as we discussed in Section 5.1.2, our estimates of $N_{\mathrm{exp,0462}}$ are robust to any changes in the BH mass function as long as the total number of BHs is conserved. This is again due to the cancellation between the two factors of $\Gamma_{\mathrm{BH}}(u_0 < 0.1, t_E > 200$ days) and $P_{\mathrm{BH}}(\pi_E > 0.06 \mid t_{\mathrm{E,OB110462}})$ because of the different dependence on M_L for $t_E \propto M_L^{1/2}$ and $\pi_E \propto M_L^{-1/2}$. Olejak et al. (2020) found about 8% of BHs are in binary systems based on a population synthesis study. Although the uncertainty of the binary fraction is large, any reasonable amount of the BH binary fraction would not increase the total number of BHs significantly enough to change our conclusion.

5.2. Were We Lucky to Have the BH Event Detection?

We have so far discussed the unlikeliness of $v_{\mathrm{avg}} = 200 \, \mathrm{km \, s^{-1}}$ or $v_{\mathrm{avg}} = 400 \, \mathrm{km \, s^{-1}}$ due to their small values of $N_{\mathrm{exp,0462}}$, the expected numbers of BH events like OB110462 occurring during the OGLE-IV survey by Mróz et al. (2017) and Mróz et al. (2019). These are ∼0.04 for $v_{\mathrm{avg}} = 200 \, \mathrm{km \, s^{-1}}$ and ∼0.004 for $v_{\mathrm{avg}} = 400 \, \mathrm{km \, s^{-1}}$, which are much less than the actual number of such events, i.e., at least one. On the other hand, the $N_{\mathrm{exp,0462}}$ values for slower kick velocities are not large either. Even the value for $v_{\mathrm{avg}} = 25 \, \mathrm{km \, s^{-1}}$ is 0.48–0.92 depending on the model, but does not exceed 1. The interpretation of this is either of or a combination of the following.

The first possibility is that we were lucky to find the first isolated stellar-mass BH in such a unique parameter space. This can be tested by further observations of other BH events. If we see more BH events in a similarly unlikely parameter space, it would indicate this is not the case. This will be effectively investigated by the Nancy Grace Roman Space Telescope (Spergel et al. 2015), which will be launched by 2027 May. Sajadian & Sahu (2023) predict the masses of about 20 BHs can be measured assuming the BH fraction of 0.01% relative to the number of total objects if the Roman can fill its gap period between the first three and second three bulge seasons, even at low frequency. The number would be 400 BHs with the BH fraction of 0.2% in our model.

The second possibility is that there were modeling issues, and we missed true, more likely, values of t_E and/or π_E. This seems unlikely because several independent modeling attempts have been made for OB110462 (Mróz et al. 2022; Sahu et al. 2022; Lam & Lu 2023), all showing more or less similar estimates for t_E and π_E values. Nevertheless, it might be worth trying to include higher-order effects that have not been reported in the papers, such as a binary lens or the parallax effect, to see how much the estimates of t_E or π_E would change.

The third possibility is that there are unconsidered issues in our calculation of $N_{\mathrm{exp,0462}}$. Although we have reviewed likely uncertainties in our model in Section 5.1, there could be uncertainties in parts where we assumed robustness. One possibility is an overestimation of the detection efficiency of

the OGLE-IV survey for long-timescale single-lens events by Mróz et al. (2017, 2019), which was also pointed out by Mróz et al. (2019). Although the microlens parallax effect is usually very subtle and does not affect the detectability of single-lens events, it could sometimes cause a significant deviation from the Paczyński curve, particularly for long-timescale events with $t_E \gtrsim 100$ days (some examples are seen in Wyrzykowski et al. 2016). Meanwhile, Mróz et al. (2017, 2019) estimated the detection efficiency by embedding many artificial single-lens events and counting the number of events passing their selection criteria. Either the artificial events or the single-lens model used in the selection criteria does not include the parallax effect. This results in an overestimation of the detection efficiency for long-timescale events whose detectability could be affected by the parallax effect because the real events always have nonzero π_E values. The overestimation of the detection efficiency causes an underestimation of $N_{\mathrm{exp,0462}}$, because our $\Gamma_{\mathrm{BH}}(u_0 < 0.1, t_E > 200$ days) values have been calculated by dividing the expected value of event detection that can reproduce the OGLE-IV t_E distribution by the detection efficiency. Although the presence of an overestimation of the detection efficiency is plausible, the relative values of $N_{\mathrm{exp,0462}}$ among different v_{avg} values still hold, and it is unlikely that correcting this overestimation alone would increase the $N_{\mathrm{exp,0462}}$ values by more than 1 order of magnitude. Therefore, our conclusion that $v_{\mathrm{avg}} = 200 \, \mathrm{km \, s^{-1}}$ or $v_{\mathrm{avg}} = 400 \, \mathrm{km \, s^{-1}}$ is unlikely does not change due to this, whereas the $N_{\mathrm{exp,0462}}$ values smaller than 1 even for $v_{\mathrm{avg}} = 25 \, \mathrm{km \, s^{-1}}$ might be mitigated by this.

Another possible issue in our calculation of $N_{\mathrm{exp,0462}}$ is our selection criterion of $t_E > 200$ days. As mentioned in Section 4, the original HST program by Sahu (2009, 2012) probably selected their sample when the events were still ongoing and the t_E values were not yet finalized. As a result, four out of the five selected events (i.e., events other than OB110462) have the final t_E estimation of less than 200 days, ranging from 61 to 143 days (Lam et al. 2022). Since the exact reproduction of the selection process is almost impossible, we here apply different t_E threshold values, $t_{E,th}$, and see how much $\Gamma_{\mathrm{BH}}(u_0 < 0.1, t_E > t_{E,th})$ and consequently $N_{\mathrm{exp,0462}}$ change. Table 3 shows the results when we apply $t_{E,th} = 150$ days and 120 days instead of our fiducial application of $t_{E,th} = 200$ days. $N_{\mathrm{exp,0462}}$ becomes larger than 1 for $v_{\mathrm{avg}} = 25 \, \mathrm{km \, s^{-1}}$ when $t_{E,th} = 150$ days, and for $v_{\mathrm{avg}} = 25 \, \mathrm{km \, s^{-1}}$ and $50 \, \mathrm{km \, s^{-1}}$ when $t_{E,th} = 120$ days. Therefore, the tension between $N_{\mathrm{exp,0462}}$ value and the actual number of at least 1 would be mitigated for $v_{\mathrm{avg}} \lesssim 100 \, \mathrm{km \, s^{-1}}$ if we take $t_{E,th} = 150$ days or $t_{E,th} = 120$ days. Nevertheless, we keep $t_{E,th} = 200$ days as our fiducial application because OB110462, the only BH event actually identified, has $t_E > 200$ days, and the number of BH events increased by making $t_{E,th}$ smaller than 200 days is due to the contribution of events with $t_E < 200$ days. In any case, the $N_{\mathrm{exp,0462}}$ values for $v_{\mathrm{avg}} = 200 \, \mathrm{km \, s^{-1}}$ and $v_{\mathrm{avg}} = 400 \, \mathrm{km \, s^{-1}}$ are small compared to 1, which supports our conclusion that v_{avg} is likely to be $\lesssim 100 \, \mathrm{km \, s^{-1}}$.

5.3. Comparison with Previous Studies

There are some attempts to constrain the kick velocity of compact objects from the observations of microlensing events caused by them. For example, Andrews & Kalogera (2022) gave a constraint on the velocity of the natal kick to a BH that caused OB110462 from its inferred peculiar velocity as $\lesssim 100 \, \mathrm{km \, s^{-1}}$. Although their conclusion is similar to ours,

Table 3
Same as Table 2, but when Different t_E Thresholds Are Applied in the Calculation of $\Gamma_{BH}(u_0 < 0.1, t_E > t_{E,th})$

	Average Kick Velocity v_{avg}				
	25 km s^{-1}	50 km s^{-1}	100 km s^{-1}	200 km s^{-1}	400 km s^{-1}
	$N_{exp,0462}$ ($\Gamma_{BH} P_{BH}$)	$N_{exp,0462}$ ($\Gamma_{BH} P_{BH}$)	$N_{exp,0462}$ ($\Gamma_{BH} P_{BH}$)	$N_{exp,0462}$ ($\Gamma_{BH} P_{BH}$)	$N_{exp,0462}$ ($\Gamma_{BH} P_{BH}$)
$t_{E,th} = 200$ days[a]	**0.52** (4.9 0.11)	**0.38** (4.4 0.087)	**0.18** (3.4 0.053)	**0.042** (1.9 0.022)	**0.0040** (0.63 0.0063)
$t_{E,th} = 150$ days	**1.14** (10.8 0.11)	**0.88** (10.1 0.087)	**0.44** (8.4 0.053)	**0.11** (4.9 0.022)	**0.011** (1.8 0.0063)
$t_{E,th} = 120$ days	**1.76** (16.7 0.11)	**1.40** (16.2 0.087)	**0.74** (13.9 0.053)	**0.19** (8.7 0.022)	**0.021** (3.4 0.0063)

Note.
[a] Same as the fiducial model in Table 2, but listed for completeness.

there is a difference in that our analysis is not based on the peculiar velocity of the lens but based on statistical arguments about the event rate with observed t_E and π_E. The impact of the natal kick on compact remnants on the observations of photometric microlensing was partially investigated by Mróz & Wyrzykowski (2021). However, they assumed that all the remnants receive the same kick velocity and did not consider the effect of spatial distribution changes due to kicks. Recently, Sweeney et al. (2024) made predictions regarding gravitational microlensing phenomena caused by compact remnants taking into account changes in spatial distribution and velocity distribution in the Galaxy due to kicks. However, they conducted the analysis based on a single kick model, thus not being able to constrain kick velocities from observations. We predict the duration (t_E) and parallax (π_E) distribution of gravitational microlensing caused by BHs considering various average kick velocities, while incorporating the spatial distribution and velocity distribution of them. The influence of the kick velocity on the spatial distribution has not been considered in previous population synthesis models for microlensing such as the ones by Lam et al. (2020) or K21. Furthermore, we discuss the constraints on the kick velocity and the origin of a BH by comparing our results with the observations of OB110462. The results obtained in this study can also be applied in future observations when a large number of gravitational microlensing events are detected with the Roman telescope, for example.

6. Summary

In this paper, we have investigated how the natal kick velocity for Galactic BHs affects the microlensing event rate distribution for the BHs. We considered a Maxwell distribution for the kick velocity with averages of $v_{avg} = 25, 50, 100, 200,$ and 400 km s^{-1}, as well as the consequent inflation of the scale height and variation of the surface density of the BH disk. We found that the event rate for the disk BH lenses toward the Galactic bulge decreases as v_{avg} increases, mainly due to the velocity-dependent scale height inflation, which has not been taken into account by previous studies.

We then focused on OB110462, the only unambiguous isolated stellar-mass BH event to date. We calculated the expected number of BH events with parameters similar to OB110462 occurring during the OGLE-IV survey by Mróz et al. (2017) and Mróz et al. (2019), which is likely a larger sample than the one searched by a series of HST programs by

Sahu (2009) that discovered OB110462. Our fiducial model predicted the expected number of BH events like OB110462 as $N_{exp,0462} = 0.52, 0.38, 0.18, 0.042,$ and 4.0×10^{-3} for $v_{avg} = 25, 50, 100, 200,$ and 400 km s^{-1}, respectively, and these numbers were not sensitive to the BH mass function or the choice of models as far as we considered. The $N_{exp,0462}$ values could be underestimated because we did not consider the likely overestimation of the detection efficiency of the OGLE-IV survey for long-timescale events (Mróz et al. 2019) or the exact selection process that the original HST program applied. However, it is unlikely that the numbers would be more than 10 times larger even if the overestimation of the detection efficiency is corrected. Therefore, we concluded that the average kick velocity is likely to be $v_{avg} \lesssim 100$ km s^{-1}.

The $N_{exp,0462}$ value takes its maximum of 0.26 for the lowest kick of $v_{avg} = 25$ km s^{-1}, which still expects less than one event. This might indicate that we were lucky to discover the first BH event in such a unique parameter space, but another possibility is due to the underestimation of $N_{exp,0462}$ because of the overestimation of the detection efficiency or the application of an inappropriate selection function. The possibility of this event as a statistical fluke can be confirmed/confuted by whether or not we see more BH events in a similarly unlikely parameter space in the future.

The microlensing survey by the Nancy Grace Roman Space Telescope (Spergel et al. 2015) is capable of measuring masses of 20 BHs (Sajadian & Sahu 2023) when the BH fraction in our Galaxy is assumed to be 0.01%, and this would be 400 BHs when a 0.2% BH fraction is assumed as in our model. We can extend this study using the BH samples by the Roman survey to constrain the kick velocity distribution even tighter.

ORCID iDs

Naoki Koshimoto ⬤ https://orcid.org/0000-0003-2302-9562
Norita Kawanaka ⬤ https://orcid.org/0000-0001-8181-7511
Daichi Tsuna ⬤ https://orcid.org/0000-0002-6347-3089

References

Agol, E., & Kamionkowski, M. 2002, MNRAS, 334, 553
Agol, E., Kamionkowski, M., Koopmans, L. V. E., et al. 2002, ApJL, 576, L131
Andrews, J. J., Breivik, K., & Chatterjee, S. 2019, ApJ, 886, 68
Andrews, J. J., & Kalogera, V. 2022, ApJ, 930, 159
Andrews, J. J., Taggart, K., & Foley, R. 2022, arXiv:2207.00680
Armitage, P. J., & Natarajan, P. 1999, ApJL, 523, L7
Bailyn, C. D., Jain, R. K., Coppi, P., et al. 1998, ApJ, 499, 367
Banagiri, S., Doctor, Z., Kalogera, V., et al. 2023, ApJ, 959, 106
Barkov, M. V., Khangulyan, D. V., & Popov, S. B. 2012, MNRAS, 427, 589
Bennett, D. P., Becker, A. C., Quinn, J. L., et al. 2002, ApJ, 579, 639
Bovy, J. 2017, MNRAS, 470, 1360
Breivik, K., Chatterjee, S., & Larson, S. L. 2017, ApJL, 850, L13
Burrows, A., Vartanyan, D., & Wang, T. 2023, ApJ, 957, 68
Burrows, A., Wang, T., Vartanyan, D., et al. 2024, ApJ, 963, 63
Campana, S., & Pardi, M. C. 1993, A&A, 277, 477
Caputo, D. P., de Vries, N., Patruno, A., et al. 2017, MNRAS, 468, 4000
Carr, B. J. 1979, MNRAS, 189, 123
Chakrabarti, S., Simon, J. D., Craig, P. A., et al. 2023, AJ, 166, 6
Chawla, C., Chatterjee, S., Breivik, K., et al. 2022, ApJ, 931, 107
Chisholm, J. R., Dodelson, S., & Kolb, E. W. 2003, ApJ, 596, 437
Clarke, J. P., Wegg, C., Gerhard, O., et al. 2019, MNRAS, 489, 3519
Corral-Santana, J. M., Casares, J., Muñoz-Darias, T., et al. 2016, A&A, 587, A61
Einstein, A. 1936, Sci, 84, 506
El-Badry, K., Rix, H.-W., Quataert, E., et al. 2023a, MNRAS, 518, 1057
El-Badry, K., Rix, H.-W., Cendes, Y., et al. 2023b, MNRAS, 521, 4323
Farr, W. M., Sravan, N., Cantrell, A., et al. 2011, ApJ, 741, 103
Fender, R. P., Maccarone, T. J., & Heywood, I. 2013, MNRAS, 430, 1538
Fragos, T., Willems, B., Kalogera, V., et al. 2009, ApJ, 697, 1057
Fryer, C. L., Belczynski, K., Wiktorowicz, G., et al. 2012, ApJ, 749, 91
Fujita, Y., Inoue, S., Nakamura, T., et al. 1998, ApJL, 495, L85
Gaia Collaboration, Katz, D., Antoja, T., et al. 2018, A&A, 616, A11
Gaia Collaboration, Panuzzo, P., Mazeh, T., et al. 2024, A&A, 686, L2
Gandhi, P., Rao, A., Charles, P. A., et al. 2020, MNRAS, 496, L22
Gould, A. 2000, ApJ, 535, 928
Grindlay, J. E. 1978, ApJ, 221, 234
Hobbs, G., Lorimer, D. R., Lyne, A. G., et al. 2005, MNRAS, 360, 974
Hog, E., Novikov, I. D., & Polnarev, A. G. 1995, A&A, 294, 287
Igoshev, A. P. 2020, MNRAS, 494, 3663
Igoshev, A. P., Chruslinska, M., Dorozsmai, A., et al. 2021, MNRAS, 508, 3345
Ioka, K., Matsumoto, T., Teraki, Y., et al. 2017, MNRAS, 470, 3332
Janka, H.-T. 2013, MNRAS, 434, 1355
Janka, H.-T., & Kresse, D. 2024, arXiv:2401.13817
Jonker, P. G., Kaur, K., Stone, N., et al. 2021, ApJ, 921, 131
Kains, N., Calamida, A., Sahu, K. C., et al. 2017, ApJ, 843, 145
Kawanaka, N., Yamaguchi, M., Piran, T., et al. 2017, in IAU Symp. 324, New Frontiers in Black Hole Astrophysics, ed. A. Gomboc (Cambridge: Cambridge Univ. Press), 41
Kimball, C., Imperato, S., Kalogera, V., et al. 2023, ApJL, 952, L34
Kimura, S. S., Kashiyama, K., & Hotokezaka, K. 2021, ApJL, 922, L15
Kinugawa, T., & Yamaguchi, M. S. 2018, arXiv:1810.09721
Koshimoto, N., Baba, J., & Bennett, D. P. 2021, ApJ, 917, 78
Koshimoto, N., & Ranc, C. 2022 nkoshimoto/genulens: Release version 1.2, v1.2, Zenodo, doi:10.5281/zenodo.4784948
Kunder, A., Koch, A., Rich, R. M., et al. 2012, AJ, 143, 57
Lai, D., Chernoff, D. F., & Cordes, J. M. 2001, ApJ, 549, 1111
Lam, C. Y., & Lu, J. R. 2023, ApJ, 955, 116

Lam, C. Y., Lu, J. R., Hosek, M. W., et al. 2020, ApJ, 889, 31
Lam, C. Y., Lu, J. R., Udalski, A., et al. 2022, ApJL, 933, L23
Lam, C. Y., Lu, J. R., Udalski, A., et al. 2022, ApJS, 260, 55
Lamberts, A., Garrison-Kimmel, S., Hopkins, P. F., et al. 2018, MNRAS, 480, 2704
Lu, J. R., Sinukoff, E., Ofek, E. O., et al. 2016, ApJ, 830, 41
Maccarone, T. J. 2005, MNRAS, 360, L30
Mashian, N., & Loeb, A. 2017, MNRAS, 470, 2611
Matsumoto, T., Teraki, Y., & Ioka, K. 2018, MNRAS, 475, 1251
McDowell, J. 1985, MNRAS, 217, 77
Meszaros, P. 1975, A&A, 44, 59
Mii, H., & Totani, T. 2005, ApJ, 628, 873
Miyamoto, M., & Yoshii, Y. 1995, AJ, 110, 1427
Mróz, P., Udalski, A., Skowron, J., et al. 2017, Natur, 548, 183
Mróz, P., Udalski, A., Skowron, J., et al. 2019, ApJS, 244, 29
Mróz, P., Udalski, A., & Gould, A. 2022, ApJL, 937, L24
Mroz, P., Udalski, A., Wyrzykowski, L., et al. 2021, arXiv:2107.13697
Mróz, P., & Wyrzykowski, Ł. 2021, AcA, 71, 89
Nataf, D. M., Gould, A., Fouqué, P., et al. 2013, ApJ, 769, 88
Olejak, A., Belczynski, K., Bulik, T., et al. 2020, A&A, 638, A94
Özel, F., Psaltis, D., Narayan, R., et al. 2010, ApJ, 725, 1918
Paczynski, B. 1986, ApJ, 304, 1
Perkins, S. E., McGill, P., Dawson, W., et al. 2024, ApJ, 961, 179
Popov, S. B., & Prokhorov, M. E. 1998, A&A, 331, 535
Raithel, C. A., Sukhbold, T., & Özel, F. 2018, ApJ, 856, 35
Rich, R. M., Reitzel, D. B., Howard, C. D., et al. 2007, ApJL, 658, L29
Rose, S., Lam, C. Y., Lu, J. R., et al. 2022, ApJ, 941, 116
Sahu, K. 2009, HST Proposal, 11707
Sahu, K. 2011, HST Proposal, 12670
Sahu, K. 2012, HST Proposal, 12986
Sahu, K. C., Anderson, J., Casertano, S., et al. 2017, Sci, 356, 1046
Sahu, K. C., Anderson, J., Casertano, S., et al. 2022, ApJ, 933, 83
Sajadian, S., & Sahu, K. C. 2023, AJ, 165, 96
Samland, M. 1998, ApJ, 496, 155
Sartore, N., & Treves, A. 2010, A&A, 523, A33
Shahaf, S., Bashi, D., Mazeh, T., et al. 2023, MNRAS, 518, 2991
Shao, Y., & Li, X.-D. 2019, ApJ, 885, 151
Shapiro, S. L., & Teukolsky, S. A. 1983, Black Holes, White Dwarfs and Neutron Stars. The Physics of Compact Objects (New York: Wiley), 1983
Shikauchi, M., Kumamoto, J., Tanikawa, A., et al. 2020, PASJ, 72, 45
Shikauchi, M., Tanikawa, A., & Kawanaka, N. 2022, ApJ, 928, 13
Shikauchi, M., Tsuna, D., Tanikawa, A., & Kawanaka, N. 2023, ApJ, 953, 52
Shvartsman, V. F. 1971, SvA, 15, 377
Smith, L. C., Lucas, P. W., Kurtev, R., et al. 2018, MNRAS, 474, 1826
Spergel, D., Gehrels, N., Baltay, C., et al. 2015, arXiv:1503.03757
Sukhbold, T., Ertl, T., Woosley, S. E., et al. 2016, ApJ, 821, 38
Sweeney, D., Tuthill, P., Krone-Martins, A., et al. 2024, MNRAS, 531, 2433
Sweeney, D., Tuthill, P., Sharma, S., et al. 2022, MNRAS, 516, 4971
Tanikawa, A., Hattori, K., Kawanaka, N., et al. 2023, ApJ, 946, 79
Tsuna, D., Kawanaka, N., & Totani, T. 2018, MNRAS, 477, 791
Tsuna, D., & Kawanaka, N. 2019, MNRAS, 488, 2099
van den Heuvel, E. P. J. 1992, Environment Observation and Climate Modeling Through International Space Projects (Noordwijk: ESA), 29
van der Kruit, P. C., & Freeman, K. C. 2011, ARA&A, 49, 301
Vigna-Gómez, A., & Ramirez-Ruiz, E. 2023, ApJL, 946, L2
Walker, M. A. 1995, ApJ, 453, 37
Wiktorowicz, G., Lu, Y., Wyrzykowski, Ł., et al. 2020, ApJ, 905, 134
Willems, B., Henninger, M., Levin, T., et al. 2005, ApJ, 625, 324
Wong, T.-W., Valsecchi, F., Ansari, A., et al. 2014, ApJ, 790, 119
Wong, T.-W., Valsecchi, F., Fragos, T., et al. 2012, ApJ, 747, 111
Wyrzykowski, Ł., & Mandel, I. 2020, A&A, 636, A20
Wyrzykowski, Ł., Kostrzewa-Rutkowska, Z., Skowron, J., et al. 2016, MNRAS, 458, 3012
Yalinewich, A., Beniamini, P., Hotokezaka, K., et al. 2018, MNRAS, 481, 930
Yamaguchi, M. S., Kawanaka, N., Bulik, T., et al. 2018, ApJ, 861, 21
Zhao, Y., Gandhi, P., Dashwood Brown, C., et al. 2023, MNRAS, 525, 1498